

# Multi-band reflectance and shadowing of RX J1604.3-2130 protoplanetary disk in scattered light<sup>★</sup>

Huisheng Zhong (钟惠生) <sup>1,2</sup>, Bin B. Ren (任彬)<sup>★★</sup> <sup>3,4,5</sup>, Bo Ma (马波) <sup>1,2</sup>, Chen Xie (谢晨) <sup>6,7</sup>, Jie Ma (马颢) <sup>8</sup>, Nicole L. Wallack <sup>9,10</sup>, Dimitri Mawet <sup>5,11</sup>, and Garreth Ruane <sup>11</sup>

<sup>1</sup> School of Physics and Astronomy, Sun Yat-sen University, Zhuhai, Guangdong 519082, China; mabo8@mail.sysu.edu.cn

<sup>2</sup> Center of CSST in the great bay area, Sun Yat-sen University, Zhuhai, Guangdong 519082, China

<sup>3</sup> Université Côte d'Azur, Observatoire de la Côte d'Azur, CNRS, Laboratoire Lagrange, Bd de l'Observatoire, CS 34229, 06304 Nice cedex 4, France; e-mail: bin.ren@oca.eu

<sup>4</sup> Université Grenoble Alpes, CNRS, Institut de Planétologie et d'Astrophysique (IPAG), F-38000 Grenoble, France

<sup>5</sup> Department of Astronomy, California Institute of Technology, MC 249-17, 1200 E California Blvd, Pasadena, CA 91125, USA

<sup>6</sup> Department of Physics and Astronomy, The Johns Hopkins University, 3701 San Martin Drive, Baltimore, MD 21218, USA

<sup>7</sup> Aix Marseille Univ., CNRS, CNES, LAM, Marseille, France

<sup>8</sup> Institute for Particle Physics and Astrophysics, ETH Zürich, Wolfgang Pauli Strasse 17, 8093 Zurich, Switzerland

<sup>9</sup> Earth and Planets Laboratory, Carnegie Institution for Science, Washington, DC 20015, USA

<sup>10</sup> Division of Geological & Planetary Sciences, California Institute of Technology, MC 150-21, Pasadena, CA 91125, USA

<sup>11</sup> Jet Propulsion Laboratory, California Institute of Technology, 4800 Oak Grove Dr, Pasadena, CA, 91109, USA

Received 07 December 2023; revised 01 February 2024; accepted 08 February 2024

## ABSTRACT

**Context.** Spatially-resolved circumstellar disk spectrum and composition can provide valuable insights into the bulk composition of forming planets, as well as the mineralogical signatures that emerge during and after planet formation.

**Aims.** We aim to systemically extract the RX J1604.3-213010 (J1604 hereafter) protoplanetary disk in high-contrast imaging observations, and obtain its multi-band reflectance in visible to near-infrared wavelengths.

**Methods.** We obtained coronagraphic observations of J1604 from the Keck Observatory's NIRC2 instrument, and archival data from the Very Large Telescope's SPHERE instrument. Using archival images to remove star light and speckles, we recovered the J1604 disk and obtained its surface brightness using forward modeling. Together with polarization data, we obtained the relative reflectance of the disk in  $R$ ,  $J$ ,  $H$  ( $H2$  and  $H3$ ),  $K$  ( $K1$  and  $K2$ ), and  $L'$  bands spanning two years.

**Results.** Relative to the J1604 star, the resolved disk has a reflectance of  $\sim 10^{-1}$  arcsec<sup>-2</sup> in  $R$  through  $H$  bands and  $\sim 10^{-2}$  arcsec<sup>-2</sup> in  $K$  and  $L'$  bands, showing a blue color. Together with other systems, we summarized the multi-band reflectance for 9 systems. We also identified varying disk geometry structure, and a shadow that vanished between June and August in 2015.

**Conclusions.** Motivated by broad-band observations, the deployment of cutting-edge technologies could yield higher-resolution reflection spectra, thereby informing the dust composition of disks in scattered light in the future. With multi-epoch observations, variable shadows have the potential to deepen insights into the dynamic characteristics of inner disk regions.

**Key words.** protoplanetary disks – stars: imaging – planets and satellites: detection – techniques: high angular resolution

## 1. Introduction

Over 5000 exoplanets have been found with different observational techniques to date,<sup>1</sup> and the diversity in their size and mass distribution demonstrates the variety of the formation and evolution processes of planetary systems. Planets are formed within circumstellar disks around stars, implying that all are made from gas and dust inherited from the same molecular cloud. They could thus share similar bulk composition (e.g., Wang et al. 2020a), suggesting that the composition of planets, disks, and stars are correlated. However, planets can form from different mechanisms, primarily through core accretion (e.g., Pollack et al. 1996) and disk gravitational instability (e.g., Pollack

et al. 1996; Piso & Youdin 2014; Piso et al. 2015), and these models predict different planetary luminosity and spectra (e.g., Spiegel & Burrows 2012). An investigation into the compositional makeup of planetary systems – including planets and disks – can contribute to our understanding of these celestial bodies, offering an opportunity to empirically test prevailing theories of planet formation.

Various indirect techniques were proposed to infer the bulk composition of exoplanets. Typically, mass-radius measurements of exoplanets are employed to estimate the planetary bulk composition (e.g., Zeng et al. 2019; Miller & Fortney 2011; Thorngren et al. 2016; Müller et al. 2020; Plotnykov & Valencia 2020; Adibekyan et al. 2021). The uncertainties in exoplanet property measurements, including radius and mass are however large (e.g., Weiss & Marcy 2014). In addition, the uncertainties or degeneracy from theory predictions are significant (Müller et al. 2020; Müller & Helled 2023; Rogers & Seager

<sup>★</sup> FITS images for Fig. 1 are only available at the CDS via anonymous ftp to cdsarc.cds.unistra.fr (130.79.128.5) or via <https://cdsarc.cds.unistra.fr/viz-bin/cat/J/A+A/>

<sup>★★</sup> Marie Skłodowska-Curie Fellow

<sup>1</sup> <https://exoplanetarchive.ipac.caltech.edu/>

2010; Dressing et al. 2015). Consequently, they can not precisely constrain the bulk composition of exoplanets.

Planet migration plays a decisive role in the evolution of rings and planets: the remnant planetesimal belts are candidates for cold debris discs (e.g., Jiang & Ormel 2023). Morbidelli et al. (2016) showed that accretionary processes play a major role in determining a planet’s bulk composition and volatile budget. In the case of young planets still embedded in protoplanetary disks, it thus might be possible to probe the planetary composition by obtaining the dust composition of the disks with a speculative hypothesis about migration and precise numerical simulations of accretion (Pacetti et al. 2022; Mah et al. 2023). Therefore, extracting disk composition might contribute to the confirmation of the composition of exoplanets. Characterizing the initial elemental budget contained in the protoplanetary disks from which giant planets are born could thus provide constraints to inform planet formation models (Turrini et al. 2021; Pacetti et al. 2022).

Existing studies have attempted inferring the potential composition of circumstellar disks (e.g., protoplanetary, debris). With broadband photometry, Debes et al. (2008) found that the HR 4796 debris ring might be explained using 1.4  $\mu\text{m}$ -radius grains of complex organic material; Rodigas et al. (2015) found that silicates and organics are more generally favored over water ice for HR 4796, which showed possible existence of common constituents of both interstellar and solar system comets. Using integral field spectroscopy, Bhowmik et al. (2019) observed HD 32297 with Spectro-Polarimetric High-contrast Exoplanet REsearch (SPHERE; Beuzit et al. 2019) in  $Y$ ,  $J$ , and  $H$  bands in total intensity and found that the spectral reflectance of the debris disk features a “gray to blue” color, and interpreted that it resulted from the presence of grains far below the blowout size. With a dip observed at the ice feature around 3.1  $\mu\text{m}$ , certain young disks showed potential presence of water ice, including HD 142527 (Honda et al. 2009), HD 100546 (Honda et al. 2016), AB Aur (Betti et al. 2022), and HD 141569 (Kueny et al. 2024). For HD 141569, Singh et al. (2021) found a mild negative slope and a absorption feature at around 1.5  $\mu\text{m}$ , potentially caused by the OH bonding resonance, in the reflectance across  $Y$ – $K_2$  bands. For complex circumstellar structures (e.g., spirals), a proper extraction of their morphology and reflectance is still challenging (e.g., Olofsson et al. 2023; Ren 2023), since most existing algorithms suffer from overfitting or self-subtraction, which limit a proper recovery of disk signals in high-contrast imaging observations.

To properly recover disk images to study their reflectance in an early stage of disk evolution, here we study the RX J1604.3-2130A (J1604 hereafter) disk in multiple wavelengths in scattered light with forward modeling. J1604 is a  $K2 \pm 1$  star (Preibisch & Feigelson 2005) located at a distance of  $145.3 \pm 0.6$  pc (Gaia Collaboration et al. 2023) with a mass of  $1.46^{+0.19}_{-0.35} M_{\odot}$  (Fouesneau et al. 2022) and an age of  $11 \pm 3$  Myr (Pecaut et al. 2012). Woitke et al. (2019) modeled the spectral energy distribution (SED) of J1604, showing an infrared (IR) excess of  $0.18 L_{\odot}$  for  $\lambda > 6.72 \mu\text{m}$  for a stellar luminosity of  $L_{\star} = 0.76 L_{\odot}$ . The transition outer disk around the star is nearly face-on ( $6^{\circ}$  inclination, Dong et al. 2017), and massive with a dust mass of  $\sim 40$ – $50 M_{\oplus}$  (Barenfeld et al. 2016; Pinilla et al. 2018a). There is evidence of planet-induced dust filtration (Rice et al. 2006; Canovas et al. 2017). Köhler et al. (2000) found that J1604 has a stellar companion located at  $\sim 2300$  au, itself being a binary with a 13 au separation. Davies (2019) calculated the misaligned angle between the stars’ rotation axis and the outer regions of this transitional disk ( $|i_{\star} - i_{\text{disk}}| > 52^{\circ}$ ) at the  $1.6\sigma$  level. In addition, new measurements of the projected rotational velocity ( $v \sin i$ )

indicated that the star is aligned with the inner disk, and thus misaligned with the outer disk (Sicilia-Aguilar et al. 2020).

The outer disk has a deep resolved gas cavity that is smaller than the dust cavity (van der Marel et al. 2015). The disk of J1604 was resolved with the Atacama Large Millimeter/submillimeter Array (ALMA; Mayama et al. 2018), in which the observations are indicative of a misaligned inner disk with respect to the outer disk. Considering the high-resolution continuum study of inner disks using ALMA, Francis & van der Marel (2020) measured the dust mass, which gave an upper limit of  $0.013 M_{\oplus}$  for the inner disk. Stadler et al. (2023) modeled  $^{12}\text{CO}$  intensity channel maps of the disk around J1604 and then obtained the position angle of the semimajor axis of the disk on the redshifted side ( $\theta_{\text{PA}} = 258^{\circ}.7$ ), and suggested that another massive companion – presumably orbiting with a significant inclination – shapes the inner region spanning  $\sim 0''.25$  ( $\sim 35$  au) based on localized non-Keplerian feature.

In circumstellar disk systems, the misalignment between the inner disk and the outer disk could cast shadows on the outer disk, see Bohn et al. (2022) for observation examples. Multi-epoch spectroscopic and near-infrared photometric observations reveal variability over several months, potentially linked to the instabilities or the perturbations within the inner disk (Sitko et al. 2012). In particular, changes in the shape, location and brightness of the shadow features provide valuable insights into the structure, and variability timescale of the dust casting shadow. For SAO 206462, Stolker et al. (2016) witnessed varying shadow features, which may be caused by a local perturbation of the inner disk or an accretion funnel flow from the inner disk onto the star. Existing high-contrast imaging observations by Pinilla et al. (2018b) found that the photometric shadows of J1604 outer disk are variable both in morphology and in location, suggesting that innermost regions are highly dynamic and thought could be evidence of a closer-in massive companion or a complex magnetic field topology. Ruane et al. (2019) observed similar features in  $L'$  band with Keck.

In comparison with  $J$ -band data in Pinilla et al. (2018b), the scatter surface appears slightly further from the star in  $L'$  band (Ruane et al. 2019), indicating the spatial segregation of dust particles sizes and lower opacities at longer wavelengths. Ma & Schmid (2022) conducted precise measurements of intrinsic radiation parameters, including fractional polarization and apparent disk albedo, and comprehensively characterized the scattering behavior of dust within the disk utilizing a transition disk model. Therefore, obtaining multi-band reflectance for J1604 presents an opportunity to enhance our capacity to probe the bulk composition of this disk, as well as confirming the variability of the shadows on the outer disk to probe the inner disk. In Sect. 2, we describe the details of the J1604 observations used in this study, and our data reduction procedure. Sect. 3 encompasses our modeling result and the reflectance derived from the observations. We explore the substructure of J1604 and discuss the limitation of the method within Sect. 4, which also features a comparative analysis of the relative reflectance between J1604 and other disks. Finally, we provide a concise summary in Sect. 5.

## 2. Observation & Data Reduction

### 2.1. Keck/NIRC2

We conducted  $L'$ -band observation of J1604 using the Keck/NIRC2 vortex coronagraph, which has a pixel size of 9.942 mas (e.g., Service et al. 2016; Mawet et al. 2019), on UT 2017 May 10 (Proposal ID: C280; PI: D. Mawet). The total integra-

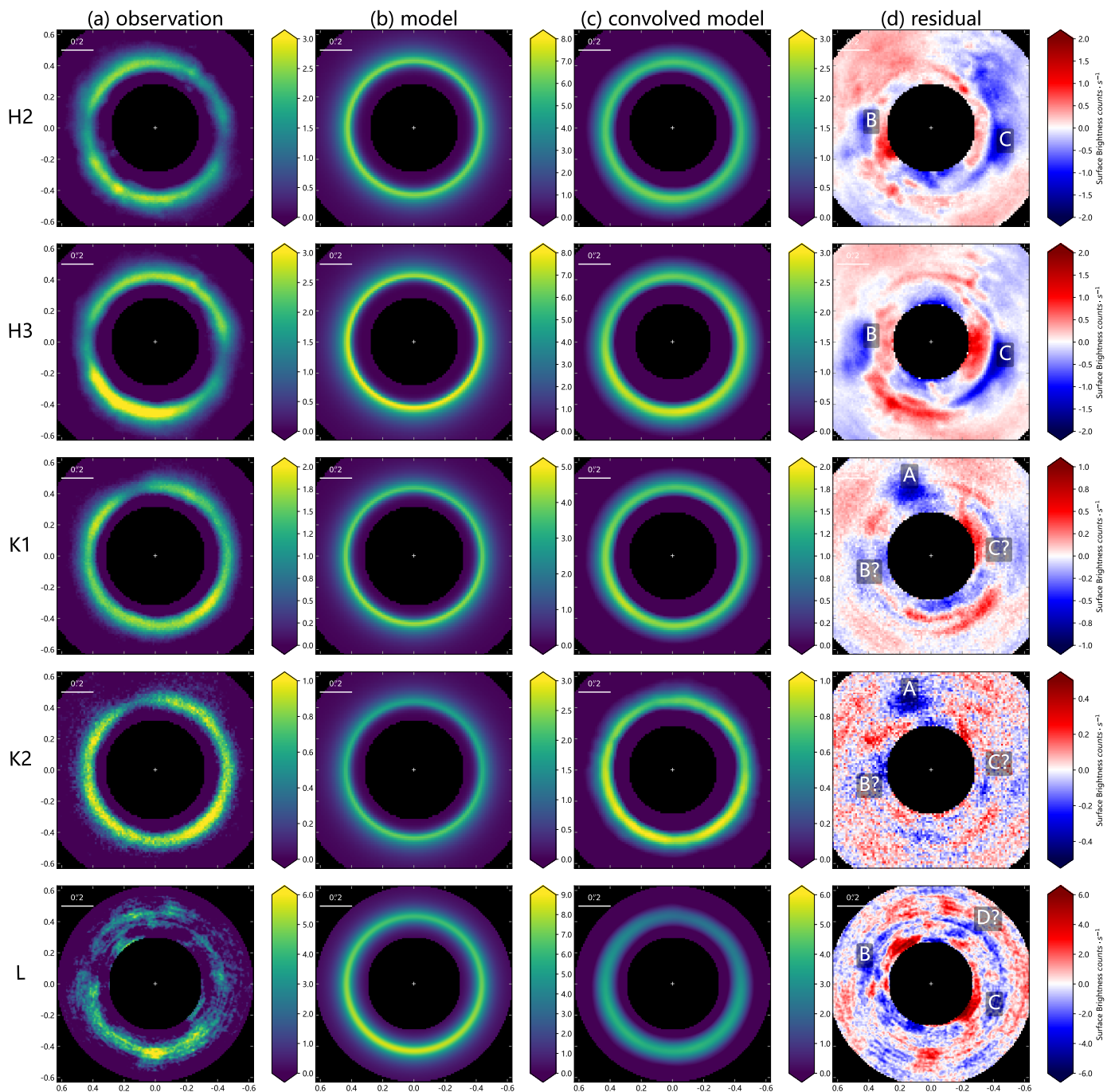


**Fig. 1.** (a) The observation of J1604 after subtracting the stellar speckles. (b) The best-fitting model. (c) The corresponding best-fitting model convolved with PSF and subtracted by the stellar speckles components. (d) The residual images after removing the best-fitting model and the stellar speckles components, see Sect. 3.1. The corresponding bands from top to bottom images are *H2* and *H3* (2015 Aug 13), *K1* and *K2* (2015 Jun 10), and *L* (2017 May 10). Numerical labels indicate the position of potential shadow features in the disk in Sect. 4.3.2.

tion time was 3285 s ( $=1 \text{ s} \times 45 \text{ coadds} \times 73 \text{ frames}$ ). During the observation, the parallactic angle rotation was  $36^\circ.2$ . In this work, we derotated the images to align the disk and then median-combined the different exposure frames, and thus field rotation (i.e., parallactic angle change) allows for quasi-static noise removal. The central wavelength of the *L*-band filter is  $3.776 \mu\text{m}$ . The observing list consists of seven targets including J1604 and six other stars which we used as reference stars to remove the star light and speckles for J1604. The corresponding off-axis point spread function (PSF) was obtained by positioning the star outside the coronagraphic mask with a total exposure time of 0.75s.

We pre-processed the observation data by performing flat-filing, bad pixel correction, and background removal (Xuan et al. 2018). For post-processing, we adopted reference differential imaging (RDI): we used the Karhunen–Loève image projection algorithm (KLIP: Soummer et al. 2012) with 6 components to maximize speckle removal while presenting surface brightness and structure. The reference images were chosen from the exposure of the reference stars, selected on the basis of their cosine similarity against the pre-processed target images. To generate the 6 components, we used 73 reference images, which match the number of frames of the J1604 observation. To obtain the fi-

nal result, we de-rotated all the images to north-up and east-left based on their parallactic angles before median-combining them altogether, see Fig. 1(a).

## 2.2. VLT/SPHERE

We retrieved archival  $H$ -band infrared dual-band imager and spectrograph (IRDIS; Dohlen et al. 2008) observations of J1604 on 2015 August 13 under program (ID: 295.C-5034) and the  $K$ -band IRDIS observations data on 2015 June 10 under program (ID: 095.C-0673). IRDIS is a dual-band imager (DBI; Vigan et al. (2010)) in SPHERE that can produce simultaneous images at two nearby wavelengths, such as  $H2$ :  $1.593 \mu\text{m}$  and  $H3$ :  $1.667 \mu\text{m}$ , or  $K1$ :  $2.110 \mu\text{m}$  and  $K2$ :  $2.251 \mu\text{m}^2$ . The pixel size of IRDIS is  $12.25 \text{ mas}$  (Maire et al. 2016). During the observation, the parallactic angle rotation in  $H$ -band was  $91^\circ 9'$ , and  $140^\circ 2'$  in  $K$ -band. Each frame's exposure time of  $H$ -band and  $K$ -band is 32s. Additionally, corresponding non-coronagraphic stellar PSF was obtained with a neutral density filter ND2 and an exposure time of 0.8375s. We employed the reference library from Xie et al. (2022) to improve the performance of RDI.

We pre-processed the raw data using the `vlt-sphere`<sup>3</sup> pipeline (Vigan 2020) to apply dark, flat, and bad pixel corrections to both the coronagraphic images and the non-coronagraphic stellar PSF image. The images were aligned using the satellite spots. Similarly to the procedure employed for the NIRC2  $L'$ -band observations, we selected the reference images exhibiting the highest correlation with the images of J1604, and image numbers match the number of frames of the target observation data. We then performed data reduction using KLIP. We de-rotated the images based on their parallactic angles and then median-combined the all frames in each filter. The resulting images are shown in Fig. 1.

## 3. Analysis and Results

### 3.1. Forward Modeling

To recover the surface brightness of J1604 disk in the 5 filters, we adopted the forward modeling technique (e.g., Mazoyer et al. 2020). In one band, we injected a negative disk model to the pre-processed data, then performed KLIP with reference differential imaging to minimize the residuals. The reduction parameters are identical to Sect. 2.

We used a static and geometric disk model to analytically describe the spatial distribution of the scatterers within the disk: we adopted the three-dimensional distribution function in cylindrical coordinates from Augereau et al. (1999):

$$n(r, z) \propto \left[ \left( \frac{r}{r_c} \right)^{-2\alpha_{\text{in}}} + \left( \frac{r}{r_c} \right)^{-2\alpha_{\text{out}}} \right]^{-\frac{1}{2}} \exp \left[ - \left( \frac{z}{hr} \right)^2 \right], \quad (1)$$

where  $h$  is the scale height,  $r_c$  is the critical radius,  $\alpha_{\text{in}} > 0$  and  $\alpha_{\text{out}} < 0$  are the asymptotic power law indices when  $r \ll r_c$  and  $r \gg r_c$ , respectively. We adopted  $h = 0.04$  from the vertical structure study of Thébaud (2009), since it is not constrained for face-on systems and we only focus on the surface brightness of the disk in this study.

Two specific angle values of the disk are needed in the modeling process, the inclination angle and the position angle. The

inclination angle ( $\theta_{\text{inc}}$ ) is defined as the dihedral angle between the disk mid-plane and the sky and the position angle ( $\theta_{\text{PA}}$ ) is defined as the position angle of the disk's semi-major axis measured from North to East. This semi-major axis is chosen as the one  $90^\circ$  counterclockwise from the semi-minor axis that is closer to Earth. For these two angles, we adopted fixed values from the analysis of ALMA observation data by Dong et al. (2017) and Stadler et al. (2023), with  $\theta_{\text{inc}} = 6^\circ$  and  $\theta_{\text{PA}} = 258^\circ 7'$ .

The scattering angle is defined as the angle measured from the incident light ray to the outgoing ray. The intensity of scattered light as a function of scattering angle is referred as scattering phase function (SPF). In this study, we adopt the parametric SPF in Henyey & Greenstein (1941) in total intensity:

$$I_{\text{tot}}(\theta) = \frac{1 - g^2}{4\pi(1 + g^2 - 2g \cos \theta)^{3/2}}, \quad (2)$$

where  $\theta$  is the scattering angle, and  $g \in (-1, 1)$  is the scattering asymmetry parameter with  $-1 < g < 0$  for backward scattering and  $0 < g < 1$  for forward scattering.

We combined the static geometric disk model with their corresponding scattering phase function to obtain a model image. To match the brightness of the disk model image with the observation data, we introduced a multiplicative scaling factor, which was raised to powers of 10 then multiplied with the disk model images. In this work, we used the `DebrisDiskFM` package (Ren et al. 2019) for disk image modeling using the Millar-Blanchaer et al. (2015) codes which have been adopted in modeling ring-like structures in debris disks and protoplanetary disks (e.g., Wang et al. 2020b; Quiroz et al. 2022; Ren et al. 2023). Recognizing the potential misalignment between the image center of simulated data and observation data due to the instrument jitter or inaccuracies in the pre-processing procedures, we adopted two parameters  $\Delta x$  and  $\Delta y$  to represent the shifts of the disk along the south-north direction and east-west direction, respectively. Due to the low S/N of the  $L'$ -band data, we set both shifts to zero when modeling the  $L'$ -band data.

To produce an observed disk model through finite telescope aperture, we rotated the model image generated from `DebrisDiskFM` package based on the parallactic angle corresponding to each of the observation images and convolved it with the normalized PSFs obtained in Sect. 2. Given the distinctive characteristics of the NIRC2 instrument, we also applied a transmission map of the NIRC2 vortex coronagraph (e.g., Wang et al. 2020b; Quiroz et al. 2022) during the  $L'$ -band modeling. We then subtracted the disk model images from the target images (i.e., negative injection) based on the corresponding parallactic angles, and removed the stellar speckles using KLIP (see Sect. 2) to obtain the residual images. We calculated the element-wise median and standard deviation of the derotated residuals to obtain the final result for negative injection.

The residual images have significantly smaller standard deviation values in the edge region, we thus excluded the edge region in our analysis. To obtain the best-fit models for the observed data, we maximized the log-likelihood function assuming independent Gaussian distribution for the final negative injection result:

$$\ln L(\Theta | X_{\text{obs}}) = -\frac{1}{2} \sum_{i=1}^N \left( \frac{X_{\text{res},i}}{\sigma_{\text{res},i}} \right)^2 - \sum_{i=1}^N \ln \sigma_{\text{res},i} - \frac{N}{2} \ln(2\pi), \quad (3)$$

where  $\Theta$  is the set of the disk and offset parameters (i.e.,  $\theta_{\text{inc}}$ ,  $\theta_{\text{PA}}$ ,  $\alpha_{\text{in}}$ ,  $\alpha_{\text{out}}$ ,  $r_c$ ,  $g$ ,  $f_{\text{flux}}$ ,  $\Delta x$ ,  $\Delta y$ ),  $X_{\text{res}}$  is the element-wise median derived from residual images across diverse exposure

<sup>2</sup> <https://www.eso.org/sci/facilities/paranal/instruments/sphere/inst/filters.html>

<sup>3</sup> <https://github.com/avigan/SPHERE>, version 1.4.2.

frames with  $N$  pixels,  $\sigma$  is the uncertainty map that has the same dimension as  $X$ . To obtain the best-fitting disk parameters for the observational data and explore the parameter space, we employed the `emcee` package (Foreman-Mackey et al. 2013). In order to reduce the influence of shadows of the disk (Pinilla et al. 2018b) during the modeling of the disk, we selectively excluded specific regions when calculating the likelihood function. This exclusion was achieved through the application of a distinctive mask as depicted in Fig. A.1.

Considering the similarity between the  $H2$  and  $H3$  band, and that signal-to-noise (S/N) of  $H3$  band is higher than  $H2$  band, we fixed the parameters  $\Delta x$  (pixel),  $\Delta y$  (pixel) of  $H2$ -band to the best parameters derived from the  $H3$  band. Similarly, in the  $K$  bands, where S/N of  $K1$  band better than  $K2$ -band, we fixed the parameters  $\Delta x$  (pixel),  $\Delta y$  (pixel) of  $K2$ -band to the optimal parameters obtained from  $K1$ -band. We presented the  $50 \pm 34$ th percentiles for the retrieved disk parameters in Table 1. We present and discuss the MCMC modeling results in appendix A.3.

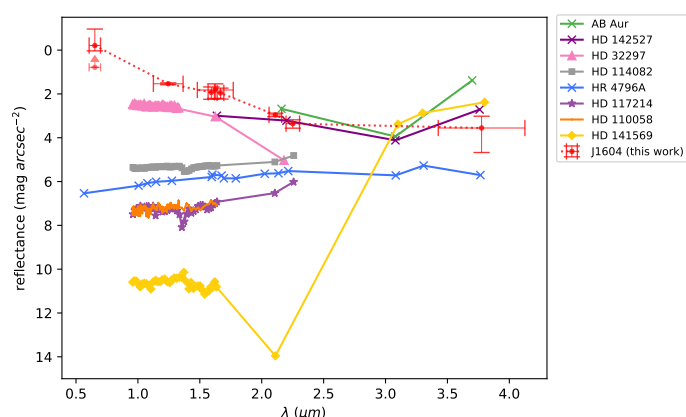


**Fig. 2.** The reflectance of different bands and different disk including HR 4796A (Debes et al. 2008; Rodigas et al. 2015; Milli et al. 2017), HD 32297 (Bhowmik et al. 2019), AB Aur (Betti et al. 2022), HD 142527 (Honda et al. 2009), HD 141569 (Singh et al. 2021; Kueny et al. 2024), HD 110058 (Stasevic et al. 2023), HD 114082 and HD 117214 (Engler et al. 2023). We scaled these disk with the square of their radial distances ratio to J1604, see Sect. 4.2. For J1604 in  $R$ -band, we only provided a lower limit for the total intensity reflectance using polarization data. Note: due to stellar activities, and thus the lag in photon arrival times between the star and the disk, the accuracy of the reflectance measurement is limited, see Sect. 4.1.

### 3.2. Aperture photometry

The effective telescope aperture of Keck II is equivalent to that of a circular aperture with a diameter of 9.96 meters.<sup>4</sup> The aperture of SPHERE is 8.0 meters in diameter seen from SPHERE (Rupprecht 2005). We obtained the host star flux, denoted as  $F_{\text{star}}$  (units: counts  $\text{s}^{-1}$ ), by integrating the image counts within the first-order diffraction ring divided by the exposure time. We set the aperture size to  $1.22 \frac{\lambda}{D}$  across all bands, to ensure that the ratio of the calculated flux to the true flux remains the same across different bands. After model fitting, we obtained a Markov chain of corresponding parameters and used it to create disk model images. We obtained average disk flux  $F_{\text{disk}}$  (units: counts  $\text{s}^{-1} \text{arcsec}^{-2}$ ) using the median pixel count number of the model image within the same aperture divided by the angular

<sup>4</sup> <https://www2.keck.hawaii.edu/observing/kecktelgde/ktelinstupdate.pdf>

size of a pixel and the exposure time. The center of aperture was placed near the position of peak surface density along the disk major axis, determined by the best-fitting disk parameter  $r_c$  and  $\theta_{\text{PA}}$ ,  $\alpha_{\text{in}}$ ,  $\alpha_{\text{out}}$  using Eq. 1. We chose this region, where the scattering angle is nearly  $90^\circ$ , to mitigate the influence of the phase function and facilitate comparisons with studies for other systems. The resulting ratio of  $F_{\text{star}}$  to  $F_{\text{disk}}$  corresponds to the reflectance  $\rho$ , expressed in units of  $\text{arcsec}^{-2}$ . This transformation effectively eliminates the influence of the stellar color and the instrument effects, enabling the quantification of the disk's reflectance  $\rho$  as a function of wavelength.

Similarly we conducted photometry on the observation data of the disk. However, it's important to note that the convolution effect of the instrument and the KLIP algorithm would influence the reflectance by introducing image blurring and reducing the surface brightness of the disk. To mitigate these effects, we divided the KLIP-reduced image by the best-fitting disk model image and subsequently mean-combined the resulting image within the region of the disk, excluding the shadows (see Fig. 1), to determine the throughput. We then corrected the reduced image by dividing it by the throughput and performed photometry on the corrected image, in this way, we can reduce the possibility that the disk model in Eq. 1 is not an accurate description of J1604 disk morphology in calculating the reflectance. This additional photometry step also allowed us to assess the accuracy of the reflectance obtained from the disk model (see Fig. A.2). When the values of the reflectance respectively obtained from the corrected image and the model image are in close agreement, we consider the results reliable.

The band widths of  $H2$ -band,  $H3$ -band,  $K1$ -band,  $K2$ -band and  $L'$ -band are 0.052, 0.054, 0.102, 0.109  $\mu\text{m}$  (Wahhaj et al. 2022), and 0.7  $\mu\text{m}$ <sup>5</sup>, respectively. Furthermore, we calculated the errors in reflectance  $\rho$  by combining the uncertainties of the stellar flux and the disk flux:

$$\begin{cases} \rho = \frac{F_{\text{disk}}}{F_{\text{star}}} \\ \left(\frac{\delta\rho}{\rho}\right)^2 = \left(\frac{\delta F_{\text{disk}}}{F_{\text{disk}}}\right)^2 + \left(\frac{\delta F_{\text{star}}}{F_{\text{star}}}\right)^2 \end{cases} \quad (4)$$

where  $\delta F_{\text{disk}}$  for modeled disk image was calculated using the Markov chain of model fitting. We corrected the residual image, as shown in Fig. 1, by dividing it by the throughput and performed photometry on the corrected image out of the disk region to obtain  $\delta F_{\text{disk}}$ .

We provided detailed aperture photometry results in Table 2. The final results, as shown in Fig. A.2 and Fig. 2, reveal that the disk scatters less light in longer wavelengths compared to shorter wavelengths. By analyzing the reflectance at various wavelengths, future work might constrain physical properties of the dust population, including size, shape and composition of the micron-sized dust particles.

## 4. Discussion

### 4.1. Stellar brightness variation

J1604 is a young active ‘dipper’ star, which exhibits quasi-periodic or aperiodic dimming events in its optical and infrared light curves. An analysis of the three known dippers with publicly available resolved sub-mm data, conducted by Ansdell et al.

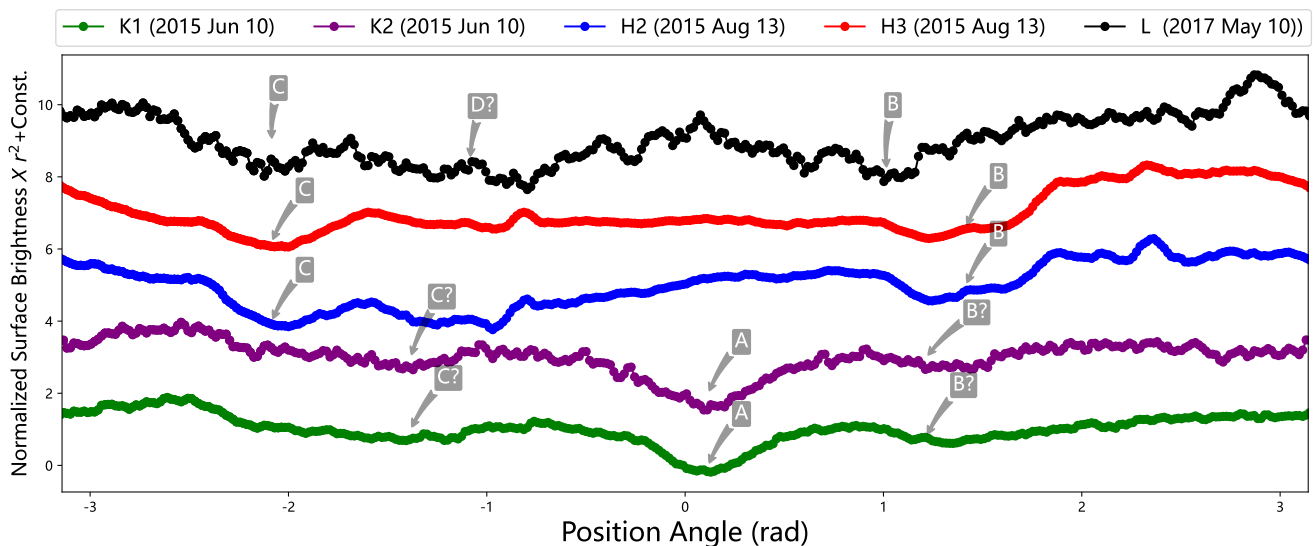
<sup>5</sup> <https://www2.keck.hawaii.edu/inst/nirc2/filters.html>

**Table 1.** Best-fitting parameters for J1604 disk in total intensity in scattered light

parameter	unit	<i>H2</i> band	<i>H3</i> band	<i>K1</i> band	<i>K2</i> band	<i>L'</i> band
$\theta_{\text{inc}}^a$	°	6	6	6	6	6
$\theta_{\text{PA}}^b$	°	258.7	258.7	258.7	258.7	258.7
$\alpha_{\text{in}}$		18.578 <sup>+2.027</sup> <sub>-1.684</sub>	25.064 <sup>+1.581</sup> <sub>-1.450</sub>	21.968 <sup>+2.573</sup> <sub>-1.490</sub>	21.063 <sup>+2.714</sup> <sub>-2.486</sub>	11.493 <sup>+2.982</sup> <sub>-2.256</sub>
$\alpha_{\text{out}}$		-6.545 <sup>+0.271</sup> <sub>-0.271</sub>	-6.161 <sup>+0.090</sup> <sub>-0.101</sub>	-7.322 <sup>+0.212</sup> <sub>-0.204</sub>	-6.856 <sup>+0.402</sup> <sub>-0.427</sub>	-8.986 <sup>+1.405</sup> <sub>-1.694</sub>
$r_c$	au	60.507 <sup>+0.341</sup> <sub>-0.340</sub>	59.993 <sup>+0.154</sup> <sub>-0.147</sub>	61.682 <sup>+0.238</sup> <sub>-0.260</sub>	61.872 <sup>+0.430</sup> <sub>-0.385</sub>	65.727 <sup>+1.426</sup> <sub>-1.240</sub>
$g$		0.126 <sup>+0.041</sup> <sub>-0.046</sub>	0.277 <sup>+0.026</sup> <sub>-0.024</sub>	0.307 <sup>+0.021</sup> <sub>-0.020</sub>	0.717 <sup>+0.162</sup> <sub>-0.183</sub>	0.743 <sup>+0.173</sup> <sub>-0.200</sub>
$\Delta x^c$	pixel	0.053	0.053 <sup>+0.031</sup> <sub>-0.031</sub>	1.12 <sup>+0.05</sup> <sub>-0.04</sub>	1.12	0
$\Delta y^c$	pixel	-1.279	-1.279 <sup>+0.037</sup> <sub>-0.038</sub>	-0.26 <sup>+0.06</sup> <sub>-0.07</sub>	-0.26	0

**Notes:**
<sup>a</sup>  $\theta_{\text{inc}}$  was fixed inferred from the dust continuum (Dong et al. 2017).

<sup>b</sup>  $\theta_{\text{PA}}$  was fixed inferred from the <sup>12</sup>CO intensity channel maps of the disk (Stadler et al. 2023).

<sup>c</sup> Offset between ring center and star.  $\Delta x$  and  $\Delta y$  (Millar-Blanchaer et al. 2015) expressed in units of instrument pixels, are fixed for specific bands. For *H2*-band, we employed the best-fitting model from the *H3* band; for *K2*-band, we utilized the best-fitting from the *K3*-band; and for the *L'*-band, no offset adjustments were applied.

**Fig. 3.** To derive the azimuthal profile, we deprojected J1604 observation data, which was processed to remove stellar contributions using the KLIP method and then scaled by  $r^2$  illumination correction. Component ‘A’ vanished between 2015 Jun and Aug, while ‘B’ and ‘C’ enhanced then. One additional component ‘D’ might start appearing in 2017 May. The vertical arrangement, from bottom to top, aligns with the chronological sequence the observation period.

(2016), concluded that nearly edge-on viewing geometries of the outer disk could not explain the depth of light curves. Sicilia-Aguilar et al. (2020) studied 10 deep eclipses of J1604 and found the brightness variation in *H*-band reached 0.2 to 0.7 mag. In the *H2*- and *H3*-band observations here, the stellar flux density on the second night is nearly twice that of the first night. The seeing conditions on the first night was  $1''.65 \pm 0''.01$ , while on the second night, they were  $1''.29 \pm 0''.05$ . This discrepancy indicates the stellar flux observed on the first night was influenced by adverse weather conditions and may not be accurate. Therefore we adopted the stellar flux obtained on the second night, and conservatively used the standard deviation of the two measured flux values as the error associated with the stellar flux measurement. In other bands, we did not detect similar stellar flux variations.

The actual stellar flux variation could impact the measurements of reflectance because the photons emitted from the star arrives at the surrounding disk with a delay of several hours to a few days. For J1604, this delay is about 8 hours: the scattered

light flux variation of the disk lags behind the flux variation of the star. Any stellar flux variation happened during the observation could lead to measured fluctuations in the disk’s brightness that deviate from actual values, biasing the derived reflectance measurements. In the future, with the aim of enhancing the reliability of the reflectance of J1604, more careful treatment of the difference in light arrival-time should be performed (e.g., TESS: Stark et al. 2023).

#### 4.2. Comparison with previous works

There are a few studies focusing on measuring the broadband reflectance or reflectance spectrum for circumstellar disks. By situating the J1604 measurements in the reflectance of HR 4796A (Debes et al. 2008; Rodigas et al. 2015; Milli et al. 2017), HD 32297 (Bhowmik et al. 2019), AB Aur (Betti et al. 2022), HD 142527 (Honda et al. 2009), HD 141569 (Singh et al.

**Table 2.** Detailed values for disk surface brightness measurement

	unit	R band	J band	H band	H2 band	H3 band	K1 band	K2 band	L' band
Epoch		2015.06	2017.08	2016.06	2015.08	2015.08	2015.06	2015.06	2017.05
Wavelength	$\mu\text{m}$	$0.65 \pm 0.05$	$1.24 \pm 0.12$	$1.62 \pm 0.14$	$1.59 \pm 0.02$	$1.67 \pm 0.02$	$2.11 \pm 0.05$	$2.25 \pm 0.06$	$3.78 \pm 0.35$
Resolution <sup>a</sup>	mas	20	39	51	50	52	66	71	95
$F_{\text{star}}^{\text{b}}$	$10^3 \text{ counts s}^{-1}$	$27 \pm 1$	$367 \pm 8$	$524 \pm 77$	$190 \pm 42$	$211 \pm 45$	$263 \pm 4$	$165 \pm 2$	$1110 \pm 1$
$F_{\text{disk}}^{(\text{model})\text{c}}$	$10^2 \text{ counts s}^{-1} \text{ arcsec}^{-2}$	$131 \pm 9^{\text{f}}$	$892 \pm 28$	$980 \pm 250$	$322_{-5}^{+6}$	$348_{-3}^{+3}$	$173_{-2}^{+3}$	$75_{-2}^{+2}$	$420_{-31}^{+31}$
$F_{\text{disk}, 1}^{(\text{obs})\text{d}}$	$10^2 \text{ counts s}^{-1} \text{ arcsec}^{-2}$				$160 \pm 40$	$170 \pm 26$	$170 \pm 12$	$93 \pm 13$	$190 \pm 270$
$F_{\text{disk}, 2}^{(\text{obs})\text{e}}$	$10^2 \text{ counts s}^{-1} \text{ arcsec}^{-2}$				$384 \pm 35$	$358 \pm 26$			$470 \pm 270$

**Notes:**

<sup>a</sup> Spatial resolution obtained from  $1.22\lambda/D$ , where  $\lambda$  is the central wavelength and D is the telescope pupil size seen by the instrument.

<sup>b</sup> In both the H-band and K-band, two stellar flux images were acquired on separate nights. The mean flux in the K-band was computed based on the two observed values, with preference given to the flux from the second night, accounting for seeing conditions. And we calculated the standard deviation with two flux values the H-band and K-band considering potential stellar brightness variation. And we also computed  $\sqrt{n}$  as the photonic noise following Poisson distribution. For instance, in the case of observations in the H2 band, the photonic noise was computed as  $\sqrt{263 \times 1000 \times 0.837/0.837}$ . The overall errors in stellar flux were determined by combining the photonic noise and the standard deviation with two night flux values.

<sup>c</sup> Average disk surface brightness for the unconvolved models. And the error was calculated by the Markov chain of corresponding disk parameters obtained in the process of forward modeling.

<sup>d</sup> Average disk surface brightness for observation with throughput correction in the major axis. And the error was calculated by the residual image in the region out of the disk.

<sup>e</sup> Average disk surface brightness for observation with throughput correction out of major axis. Considering the low inclination of the disk, the scatter angle of the region is nearly  $90^\circ$ .

<sup>f</sup> The average polarized disk surface brightness for the unconvolved disk model.

2021; Kueny et al. 2024), HD 110058 (Stasevic et al. 2023), HD 114082 and HD 117214 (Engler et al. 2023), we could study both the difference and similarity between the environment in the debris disk – where giant planet formation has reached completion – and the environment within the protoplanetary disk (e.g., AB Aur, J1604, HD 142527, HD 141569) where giant planet formation is currently in progress.

Existing studies on circumstellar disks showed several features on their reflectance. Milli et al. (2017) measured the reflectance of HR 4796A from  $0.5 \mu\text{m}$  to  $4.0 \mu\text{m}$ , which showed a monotonic increase trend from  $0.5 \mu\text{m}$  to  $1.5 \mu\text{m}$  and then almost kept constant from  $1.5 \mu\text{m}$  to  $4 \mu\text{m}$ . Bhowmik et al. (2019) measured the reflectance spectrum of HD 32297 from 1 to  $1.8 \mu\text{m}$ , the spectrum exhibited a monotonically decreasing trend with wavelength, which renders the disk a gray to blue color in the *YJH* spectral range. Employing a color-color difference diagram (Inoue et al. 2008), Honda et al. (2009) discerned the existence of silicate and H<sub>2</sub>O ice grains on the surface of the disk of HD 142527 with dust size of  $\sim 1 \mu\text{m}$ . Simiraly, AB Aur and HD 141569 was observed a absorption at the ice line at  $\sim 3.1 \mu\text{m}$  (Betti et al. 2022; Kueny et al. 2024). Engler et al. (2023) found the measured reflectance spectrum of HD 117214 disk maybe indicates the presence of CO<sub>2</sub> ice as a constituent of debris material at the investigated radial distance from the star and a red color at longer wavelengths than  $1.66 \mu\text{m}$  for both HD 117214 and HD 114082.

The reflectance measurements of J1604 here encompass the broadest wavelength range from  $0.5 \mu\text{m}$  to  $4 \mu\text{m}$  to date (e.g., HR 4796A: Debes et al. 2008). Considering decrease of stellar light intensity with distance which scales as  $1/r^2$ , where  $r$  is the stellocentric distance, we scaled these disk reflectance with the square of their radial distances ratio to J1604 (e.g., the scaling factor for HD 114082 is  $r_{\text{HD114082}}^2/r_{\text{J1604}}^2 = (31 \text{ au}/61 \text{ au})^2 = 0.26$ , and HD 32297  $r_{\text{HD32297}}^2/r_{\text{J1604}}^2 = (134.7 \text{ au}/61 \text{ au})^2 = 4.88$ ). The reflectance amplitudes of the debris disk after scaling, including HR 4796A and HD 117214 and HD 114082, were at  $10^{-2}$ – $10^{-3} \text{ arcsec}^{-2}$ , signifying a lower magnitude compared

to the reflectance amplitude of protoplanetary disks including J1604, AB Aur, and HD 142527, which are at  $\sim 10^{-1} \text{ arcsec}^{-2}$ .

We can identify a monotonically decreasing trend in the reflectance of J1604 over the wavelength range of  $0.5 \mu\text{m}$  to  $2.1 \mu\text{m}$  (i.e., blue color), contrasting with the flat or gradual increase in the reflectance of HD 114082 and HD 117214, HR 4796A, HD 110058, all of which are debris disks (i.e., gray to red color). With the distance-dependent scaling, the reflectance trend of HD 32297 and HD 141569 is relatively close to J1604. It could be speculated that the evolution of the disk may entail a progressive transition in the reflectance spectrum shape, shifting from J1604-like characteristic blue slope to those featuring red slope resembling HR 4796A. Additionally, the reflectance of J1604 and HR 4796A both exhibit a consistent, flat trend within the wavelength range of  $2.1 \mu\text{m}$  to  $4 \mu\text{m}$ . In contrast, for AB Aur, HD 141569, and HD 141527 the reflectance at  $\sim 3.8 \mu\text{m}$  is larger than that at  $\sim 2.2 \mu\text{m}$  in the same wavelength span and showed potential water ice absorption. We note the necessity for additional data points of J1604 within the wavelength range of  $2.1 \mu\text{m}$  to  $4 \mu\text{m}$  to explore its corresponding features. Finally, there are potential biases in compiling and analyzing the statistical results should not be disregarded, since there are inconsistencies in existing surface brightness measuring and reporting methods in previous work. Specifically, the reflectance measurement by Singh et al. (2021), along with some other studies, utilized the average flux of the whole disk, which is different from our measurement in Sect. 3.2. A limited quantity of available samples hinders comprehensive analysis. Future studies on reflectance spectra using integral field spectrograph (IFS), including SPHERE and Gemini planet Imager (GPI), will help better probe the spectroscopic trends as well as the mineralogical composition of circumstellar disks when aided with laboratory measurements (e.g., Poch et al. 2023).

### 4.3. Varying disk structure

#### 4.3.1. Structure

The disk geometry structure which we obtained by forward-modeling vary with the wavelengths. Although the fitting parameters  $r_c$  and  $\alpha_{in}$ ,  $\alpha_{out}$  in the  $H$ -band closely resemble those in the  $K$ -band due to the proximity in wavelength, significant differences are observed in the best-fitting parameters  $r_c$  and  $\alpha_{in}$ ,  $\alpha_{out}$  for the  $L'$ -band. The significant difference in wavelength may be attributed to the spatial segregation of dust particles, which vary in size and scattering properties, potentially influenced by size-dependent forces. For example, the unitless ratio  $\beta$  between radiation pressure and gravitational forces exhibits an inverse proportionality to grain size for grains larger than a few  $\mu\text{m}$  (Olofsson et al. 2022). Additionally, the drag, which the gas exerts on the grains, is known to be size-dependent (Takeuchi & Artymowicz 2001).

In comparison to  $L'$ -band, the values of  $\alpha_{in}$  in both  $H$ -bands and  $K$ -bands are notably larger, indicating a sharper inner edge. This result suggests the possible presence of dust particles condensed at the inner edge, such as  $\text{NH}_3$ , water ice and hydrated minerals (Popa & Udra 2019),<sup>6</sup> which exhibit strong light-absorption characteristics in  $H$ -bands or  $K$ -bands but exhibit a less significant effect in the  $L'$ -band. Another explanation for the observed cavity with sharp edge in both the  $K$ -band and the  $H$ -band could involve the presence of a  $\sim 15 M_{\text{Jup}}$  brown dwarf orbiting at  $\sim 15$  au (Canovas et al. 2017). It is well-established that a massive giant planet can create a cavity with sharp edge within the disk (Pinilla et al. 2012; Johansen et al. 2019). Rodigas et al. (2014) derived a linear expression relating a shepherding planet's maximum mass to the debris ring's observed width in scattered light. Yet J1604 is not a debris system but a protoplanetary/transition disk which is rich in gas thus can involve more complex mechanisms. Future work on explaining the radial distribution of rings in protoplanetary/transition disks could better explain the observation in this study.

#### 4.3.2. Shadows

The observed asymmetry of the transition disks in the form of shadows is widely attributed to the inner disk inclined significantly relative to the outer disk, resulting in the casting of varying-depth shadows onto the outer disk (Bohn et al. 2022). Min et al. (2017) provided analytical equations describing the positions of these shadow features as a function of the orientation between the inner and outer disk and the height of the outer disk wall, such as HD100453. Based on the hydrodynamic simulations combined with three-dimensional radiative transfer calculations, Benisty et al. (2018) adopted the warped disk model and reproduced all major morphological features for HD 143006. Similarly Muro-Arena et al. (2020) found that a single misaligned ring was insufficient to account for the wide shadow and instead utilized two separate misaligned zones to effectively reproduce most of the observed features within the protoplanetary disk of HD 139614. Through a comparative analysis of STIS images in 2000 and those from NICMOS in 1998, 2004, and 2005, Debes et al. (2017) quantified a constant angular velocity in the azimuthal brightness asymmetry of the TW Hya disk, manifesting a counterclockwise direction. Recently, Debes et al. (2023) reported the presence of two distinct shadows observed in the TW Hya that changed from one in Debes et al. (2017).

We detected potential physical substructures exhibiting pixelwise average S/N exceeding 1, including two shadows, and one potential inner dust. After subtracting the best-fitting model and the stellar PSF components, we present the residual images, in Fig. 1. Specifically, we observed one round shadow and two indistinct shadows in the  $K$ -bands on 2015 June 10, respectively denoted as 'A' and 'B?', 'C?' in Fig. 1. From the observation in the  $H$ -bands on 2015 Aug 13, we identified one narrow shadow accompanied by another wider shadow, respectively denoted as 'B', 'C' in Fig. 1, both of which closely neighbored two indistinct shadows in the  $K$ -bands. Additionally, the  $L'$ -band observations on May 10, 2017, revealed the presence of two wide shadow and an additional inconspicuous shadow, respectively denoted as 'B', 'C' and 'D?' in Fig. 1. To quantify the asymmetry, we computed radially averaged azimuthal profiles of the disk reduced data, using apertures of 6 pixel in radius placed near the position of  $r_c$ , after deprojecting the image using  $\theta_{\text{inc}} = 6^\circ$  and  $\theta_{\text{PA}} = 258:7$  and scaling by its distance from the central star. The resulting figure is depicted in Fig. 3

The temporal variability of the shadows is in accordance with the findings of Pinilla et al. (2018b). In comparison to the shadow observations reported by Muro-Arena et al. (2020) and Debes et al. (2023), the shadows observed in this study have several similar dynamics features. Similarly, the number of the shadows exhibits temporal variation. Furthermore, Considering the observed data for J1604, we could infer the existence of potential multiply misaligned and dynamic rings within the inner region, which may contribute to the generation of wide and variable shadows. This inference suggests that the brighter inner side could coincide with the fainter region of the outer disk. However, unlike the two overlapping shadows reported by Debes et al. (2023), our  $H$ -band observations revealed non-overlapping shadows. In contrast to the multiple arcs feature out of the parallactic angle range of the shadow reported by Muro-Arena et al. (2020), we detected only one possible arc in the  $H3$ -band observation. Taking in account the observation by Pinilla et al. (2018b), we inferred that the shadow of J1604 occupied in 'A' position between 2012 and 2015. We confirmed the change of the shadows number from one to two occurred in 2015. It is likely that 'A' shadow disappeared in 2015, and then the shadows in B and C position gradually became evident, which was distinct from the rotation of the shadows and can not be explained by the precession of an inner disk (Debes et al. 2017). The observations here report a distinct and previously less explored dynamical characteristics of inner disks.

Due to the small dust mass and large inclination, small separation, the inner disk remains inaccessible from direct imaging instruments. We detected positive residuals interior to one shadow ('C') on the outer disk. If the signal was true, it could be residual dust right outside the coronagraph that is better revealed after disk modeling. The dust can block more light and make the shadow on the outer disk darker and wider than another shadow ('B'). While this may be a spiral running away from the inner disk due to a massive coronal mass ejection (CME) along the equatorial plane of the star (e.g., Olofsson et al. 2018), it should be noted that CME is for M stars and not applicable for J1604 which is a K2 star.

The residual images of other bands also reveal discernible shadows at varying positions, see Fig. 1. Due to the low S/N, we do not discuss more about the residual images in other bands (i.e.,  $K$ ,  $L'$ ).

<sup>6</sup> <https://www.nist.gov/>



## 5. Conclusion

We conducted  $L'$ -band observations of the J1604 protoplanetary disk system using the Keck/NIRC2 vortex coronagraph on UT 2017 May 10. We also retrieved archival SPHERE observations of J1604 on 2015 August 13 in  $H2$ - and  $H3$ -band, and on 2015 June 10 in  $K1$ - and  $K2$ -band. Using KLIP post-processing with reference differential imaging (either exposures in nearby nights for NIRC2, or archival exposures for IRDIS), we obtained the images of J1604 disk. We forward modeled the disk in different bands to obtain its original surface brightness.

Using forward modeling and comparing with stellar photometry (within  $1.22\lambda/D$ ), we obtained broadband relative reflectance for J1604 in total intensity imaging observations. Together shorter-wavelength SPHERE study in polarized light and for  $R$ - and  $H$ -band (Ma et al. 2023), our J1604 reflectance measurements span a broad wavelength range from  $0.5 \mu\text{m}$  to  $4 \mu\text{m}$ . On the one hand, from  $0.5 \mu\text{m}$  to  $2.1 \mu\text{m}$ , we observe a monotonically decreasing trend in its reflectance. This trend contrasts with previous work showing gradual increasing trend debris disks (e.g., HD 114082, HD 117214, HR 4796A), illustrating potential mineralogical difference in different evolutionary stages of circumstellar disks. The evolution of the disk might thus have a progressive transition in the reflectance spectrum shape, shifting from J1604-like characteristic blue slope to those featuring red slope resembling HR 4796A. On the other hand, from  $2.1 \mu\text{m}$  to  $4 \mu\text{m}$ , we observe a relatively flat reflectance. This differs from the phenomenon that the reflectance at  $\sim 3.8 \mu\text{m}$  is larger than that at  $\sim 2.2 \mu\text{m}$  observed in the reflectance of AB Aur, HD 142527, and HD 141569, suggesting the difference of dust mineralogy potentially due to different protoplanetary disk stage or even different molecular cloud origins. Moving forward, to further explore the trends and differences in the reflectance of circumstellar disks, future studies on reflectance spectra with integral field spectrographs (e.g., SPHERE, Gemini planet Imager) that can spatially resolve circumstellar systems are necessary.

From the shadow variation that cannot be explained by the precession of the inner disk, we are in the era of witnessing a possible, distinct and previously less explored dynamical characteristics of inner disks in protoplanetary systems (e.g., Debes et al. 2023). We identified a shadow that vanished in 2015 (labeled 'A'), and two shadow that potentially enhanced then (labeled 'B' and 'C'). Our modeling residuals show potential dust components that can cast shadows on outer disk. Future multi-epoch follow-up of outer disks in scattered light could help us probe the dynamics of the inner disks and study the connection of the two regions (e.g., Bohn et al. 2022).

**Acknowledgements.** We thank Myriam Benisty for discussions on shadowing effects, and Juan Quiroz for sharing a disk modeling example. We thank Benoit Carry, Pierre Beck, and Oliver Poch for discussions on dust reflectance. This research has received funding from the European Union's Horizon Europe research and innovation programme under the Marie Skłodowska-Curie grant agreement No. 101103114. This project has received funding from the European Research Council (ERC) under the European Union's Horizon 2020 research and innovation programme (PROTOPLANETS, grant agreement No. 101002188). We acknowledge the financial support from the National Key R&D Program of China (2020YFC2201400), NSFC grant 12073092, 12103097, 12103098, 11733006, the science research grants from the China Manned Space Project (No. CMS-CSST-2021-B09), Guangdong Major Project of Basic and Applied Basic Research (grant No. 2019B030302001), Guangzhou Basic and Applied Basic Research Program (202102080371), and the Fundamental Research Funds for the Central Universities, Sun Yat-sen University. Based on observations performed with VLT/SPHERE under program ID 095.C-0673(A) and 295.C-5034(A). This research is partially supported by NASA ROSES XRP, award 80NSSC19K0294. Some of the data presented herein were obtained at the W. M. Keck Observatory, which is operated as a scientific partnership among the California Institute of Technology, the University of California and the National Aeronautics and Space Administration. The Observatory was made possible by the generous fi-

ancial support of the W. M. Keck Foundation. The authors wish to recognize and acknowledge the very significant cultural role and reverence that the summit of Maunakea has always had within the indigenous Hawaiian community. We are most fortunate to have the opportunity to conduct observations from this mountain. Part of the computations presented here were conducted in the Resnick High Performance Computing Center, a facility supported by Resnick Sustainability Institute at the California Institute of Technology.

## References

- Adibekyan, V., Dorn, C., Sousa, S. G., et al. 2021, *Science*, **374**, 330  
 Ansdell, M., Gaidos, E., Williams, J. P., et al. 2016, *MNRAS*, **462**, L101  
 Augereau, J. C., Lagrange, A. M., Mouillet, D., et al. 1999, *A&A*, **348**, 557  
 Barenfeld, S. A., Carpenter, J. M., Ricci, L., & Isella, A. 2016, *ApJ*, **827**, 142  
 Benisty, M., Juhász, A., Facchini, S., et al. 2018, *A&A*, **619**, A171  
 Betti, S. K., Follette, K., Jorquera, S., et al. 2022, *AJ*, **163**, 145  
 Beuzit, J. L., Vigan, A., Mouillet, D., et al. 2019, *A&A*, **631**, A155  
 Bhowmik, T., Boccaletti, A., Thébault, P., et al. 2019, *A&A*, **630**, A85  
 Bohn, A. J., Benisty, M., Perraut, K., et al. 2022, *A&A*, **658**, A183  
 Canovas, H., Hardy, A., Zurlo, A., et al. 2017, *A&A*, **598**, A43  
 Davies, C. L. 2019, *MNRAS*, **484**, 1926  
 Debes, J., Nealon, R., Alexander, R., et al. 2023, *ApJ*, **948**, 36  
 Debes, J. H., Weinberger, A. J., & Schneider, G. 2008, *ApJ*, **673**, L191  
 Debes, J. H., Poteet, C. A., Jang-Condell, H., et al. 2017, *ApJ*, **835**, 205  
 Dohlen, K., Langlois, M., Saisse, M., et al. 2008, *Proc. SPIE*, **7014**, 70143L  
 Dong, R., van der Marel, N., Hashimoto, J., et al. 2017, *ApJ*, **836**, 201  
 Dressing, C. D., Charbonneau, D., Dumusque, X., et al. 2015, *ApJ*, **800**, 135  
 Engler, N., Milli, J., Gratton, R., et al. 2023, *A&A*, **672**, A1  
 Foreman-Mackey, D., Hogg, D. W., Lang, D., & Goodman, J. 2013, *PASP*, **125**, 306  
 Fouesneau, M., Andrae, R., Dharmawardena, T., et al. 2022, *A&A*, **662**, A125  
 Francis, L., & van der Marel, N. 2020, *ApJ*, **892**, 111  
 Gaia Collaboration, Vallenari, A., Brown, A. G. A., et al. 2023, *A&A*, **674**, A1  
 Henyey, L. G., & Greenstein, J. L. 1941, *ApJ*, **93**, 70  
 Honda, M., Inoue, A. K., Fukagawa, M., et al. 2009, *ApJ*, **690**, L110  
 Honda, M., Kudo, T., Takatsuki, S., et al. 2016, *ApJ*, **821**, 2  
 Inoue, A. K., Honda, M., Nakamoto, T., & Oka, A. 2008, *PASJ*, **60**, 557  
 Jiang, H., & Ormel, C. W. 2023, *MNRAS*, **518**, 3877  
 Johansen, A., Ida, S., & Brasser, R. 2019, *A&A*, **622**, A202  
 Köhler, R., Kunkel, M., Leinert, C., & Zinnecker, H. 2000, *A&A*, **356**, 541  
 Kueny, J. K., Weinberger, A. J., Males, J. R., et al. 2024, *ApJ*, **961**, 77  
 Ma, J., & Schmid, H. M. 2022, *A&A*, **663**, A110  
 Ma, J., Schmid, H. M., & Tschudi, C. 2023, *A&A*, **676**, A6  
 Mah, J., Bitsch, B., Pascucci, I., & Henning, T. 2023, *A&A*, **677**, L7  
 Maire, A.-L., Langlois, M., Dohlen, K., et al. 2016, *Proc. SPIE*, **9908**, 990834  
 Mawet, D., Hirsch, L., Lee, E. J., et al. 2019, *AJ*, **157**, 33  
 Mayama, S., Akiyama, E., Panić, O., et al. 2018, *ApJ*, **868**, L3  
 Mazoyer, J., Arriaga, P., Hom, J., et al. 2020, *Proc. SPIE*, **11447**, 1144759  
 Millar-Blanchaer, M. A., Graham, J. R., Pueyo, L., et al. 2015, *ApJ*, **811**, 18  
 Miller, N., & Fortney, J. J. 2011, *ApJ*, **736**, L29  
 Milli, J., Vigan, A., Mouillet, D., et al. 2017, *A&A*, **599**, A108  
 Min, M., Stolker, T., Dominik, C., & Benisty, M. 2017, *A&A*, **604**, L10  
 Morbidelli, A., Bitsch, B., Crida, A., et al. 2016, *Icarus*, **267**, 368  
 Müller, S., Ben-Yami, M., & Helled, R. 2020, *ApJ*, **903**, 147  
 Müller, S., & Helled, R. 2023, *FrASS*, **10**, 1179000  
 Muro-Arena, G. A., Benisty, M., Ginski, C., et al. 2020, *A&A*, **635**, A121  
 Olofsson, J., Thébault, P., Kennedy, G. M., & Bayo, A. 2022, *A&A*, **664**, A122  
 Olofsson, J., van Holstein, R. G., Boccaletti, A., et al. 2018, *A&A*, **617**, A109  
 Olofsson, J., Thébault, P., Bayo, A., et al. 2023, *A&A*, **674**, A84  
 Pacetti, E., Turrini, D., Schisano, E., et al. 2022, *ApJ*, **937**, 36  
 Peca, M. J., Mamajek, E. E., & Bubar, E. J. 2012, *ApJ*, **746**, 154  
 Pinilla, P., Benisty, M., & Birnstiel, T. 2012, *A&A*, **545**, A81  
 Pinilla, P., Tazzari, M., Pascucci, I., et al. 2018a, *ApJ*, **859**, 32  
 Pinilla, P., Benisty, M., de Boer, J., et al. 2018b, *ApJ*, **868**, 85  
 Piso, A.-M. A., & Youdin, A. N. 2014, *ApJ*, **786**, 21  
 Piso, A.-M. A., Youdin, A. N., & Murray-Clay, R. A. 2015, *ApJ*, **800**, 82  
 Plotnikov, M., & Valencia, D. 2020, *MNRAS*, **499**, 932  
 Poch, O., Istiqomah, I., Quirico, E., et al. 2023, *European Conference on Laboratory Astrophysics ECLA2020. The Interplay of Dust*, **59**, 271  
 Pollack, J. B., Hubickyj, O., Bodenheimer, P., et al. 1996, *Icarus*, **124**, 62  
 Popa, D., & Udrea, F. 2019, *Sensors*, **19**  
 Preibisch, T., & Feigelson, E. D. 2005, *ApJS*, **160**, 390  
 Quiroz, J., Wallack, N. L., Ren, B., et al. 2022, *ApJ*, **924**, L4  
 Ren, B., Choquet, É., Perrin, M. D., et al. 2019, *ApJ*, **882**, 64  
 Ren, B. 2023, *A&A*, **679**, A18  
 Ren, B. B., Rebollido, I., Choquet, É., et al. 2023, *A&A*, **672**, A114  
 Rice, W. K. M., Armitage, P. J., Wood, K., & Lodato, G. 2006, *MNRAS*, **373**, 1619

- Rodigas, T. J., Malhotra, R., & Hinz, P. M. 2014, *ApJ*, 780, 65
- Rodigas, T. J., Stark, C. C., Weinberger, A., et al. 2015, *ApJ*, 798, 96
- Rogers, L. A., & Seager, S. 2010, *ApJ*, 716, 1208
- Ruane, G., Ngo, H., Mawet, D., et al. 2019, *AJ*, 157, 118
- Rupprecht, G. 2005, Requirements for Scientific Instruments on the VLT Unit Telescopes, Tech. rep., VLT-SPE-ESO-10000-2723 publicly available at [https://www.eso.org/sci/facilities/develop/documents/VLT-SPE-ESO-10000-2723\\_is1.pdf](https://www.eso.org/sci/facilities/develop/documents/VLT-SPE-ESO-10000-2723_is1.pdf)
- Service, M., Lu, J. R., Campbell, R., et al. 2016, *PASP*, 128, 095004
- Sicilia-Aguilar, A., Manara, C. F., de Boer, J., et al. 2020, *A&A*, 633, A37
- Singh, G., Bhowmik, T., Boccaletti, A., et al. 2021, *A&A*, 653, A79
- Sitko, M. L., Day, A. N., Kimes, R. L., et al. 2012, *ApJ*, 745, 29
- Soummer, R., Pueyo, L., & Larkin, J. 2012, *ApJ*, 755, L28
- Spiegel, D. S., & Burrows, A. 2012, *ApJ*, 745, 174
- Stadler, J., Benisty, M., Izquierdo, A., et al. 2023, *A&A*, 670, L1
- Stark, C. C., Ren, B., MacGregor, M. A., et al. 2023, *ApJ*, 945, 131
- Stasevic, S., Milli, J., Mazoyer, J., et al. 2023, *A&A*, 678, A8
- Stolker, T., Dominik, C., Avenhaus, H., et al. 2016, *A&A*, 595, A113
- Takeuchi, T., & Artymowicz, P. 2001, *ApJ*, 557, 990
- Thébaud, P. 2009, *A&A*, 505, 1269
- Thorngren, D. P., Fortney, J. J., Murray-Clay, R. A., & Lopez, E. D. 2016, *ApJ*, 831, 64
- Turrini, D., Schisano, E., Fonte, S., et al. 2021, *ApJ*, 909, 40
- van der Marel, N., van Dishoeck, E. F., Bruderer, S., et al. 2015, *A&A*, 579, A106
- Vigan, A. 2020, vlt-sphere: Automatic VLT/SPHERE data reduction and analysis, Astrophysics Source Code Library, record ascl:2009.002, Astrophysics Source Code Library, record ascl:2009.002
- Vigan, A., Moutou, C., Langlois, M., et al. 2010, *MNRAS*, 407, 71
- Wahhaj, Z., Jones, M., de Rosa, R., et al. 2022, Very Large Telescope SPHERE User Manual, Tech. rep., VLT-MAN-SPH-14690-0430 publicly available at [https://www.eso.org/sci/facilities/paranal/instruments/sphere/doc/VLT-MAN-SPH-14690-0430\\_P111\\_dec\\_2022\\_zwa.pdf](https://www.eso.org/sci/facilities/paranal/instruments/sphere/doc/VLT-MAN-SPH-14690-0430_P111_dec_2022_zwa.pdf)
- Wang, J., Wang, J. J., Ma, B., et al. 2020a, *AJ*, 160, 150
- Wang, J. J., Ginzburg, S., Ren, B., et al. 2020b, *AJ*, 159, 263
- Weiss, L. M., & Marcy, G. W. 2014, *ApJ*, 783, L6
- Woitke, P., Kamp, I., Antonellini, S., et al. 2019, *PASP*, 131, 064301
- Xie, C., Choquet, E., Vigan, A., et al. 2022, *A&A*, 666, A32
- Xuan, W. J., Mawet, D., Ngo, H., et al. 2018, *AJ*, 156, 156
- Zeng, L., Jacobsen, S. B., Sasselov, D. D., et al. 2019, *PNAS*, 116, 9723

## Appendix A: Auxillary images

### A.1. The mask

In order to reduce the influence of shadows on disk modeling (e.g., Pinilla et al. 2018b), we selectively excluded specific regions when calculating the likelihood function and calculating the throughput factors. This exclusion was achieved through the application of boolean masks in Fig. A.1. Similarly, we extracted the disk reflectance at different regions to validate the measurements.

### A.2. Validation of reflectance measurements

We measured the reflectance using J1604 observation with throughput correction in two distinct regions: the first corresponds to the major axis where the scattering angle is nearly  $90^\circ$ , while the second pertains to an off-axis area to reduce the influence of shadows. We validated the consistency of the results in Fig. A.2 from different methods and Ma et al. (2023).

### A.3. MCMC modeling corner plots

We present the MCMC posteriors for H3-band in Fig. A.3. Histograms on the main diagonal show the posterior distributions for each fitted parameter marginalized over all other fitted parameters, with dashed vertical lines showing 50th percentiles. The maximum likelihood parameters are denoted using blue lines.

We observed several strong correlations among several parameters (e.g.,  $g$  and brightness scaling factor,  $\alpha_{\text{in}}$  and  $R_c$ , and  $\alpha_{\text{out}}$  and  $R_c$ ). These correlations are anticipated and can be explained given the scattering phase function and disk geometry setup in Sect. 3.1. On the one hand, the Henyey–Greenstein parameter  $g$  depicts the redistribution of light as a function of scattering angle (i.e., scattering phase function), which distributes more light to smaller scattering angles as a positive  $g$  increases in Eq. (2). It thus requires higher brightness scaling factors for larger  $g$  to reproduce the nearly face-on disk for J1604. On the other hand,  $\alpha_{\text{in}}$  and  $\alpha_{\text{out}}$  describes the asymptotic radial power law indices interior and exterior to  $R_c$ . To reproduce any disk surface brightness distribution, an increase in  $R_c$  requires the decrease in the positive  $\alpha_{\text{in}}$  (or a decrease in the negative  $\alpha_{\text{out}}$ ) to produce the surface brightness interior to (or exterior to) it in Eq. (1), since otherwise the interior regions would be too faint (or the exterior regions would be too bright).

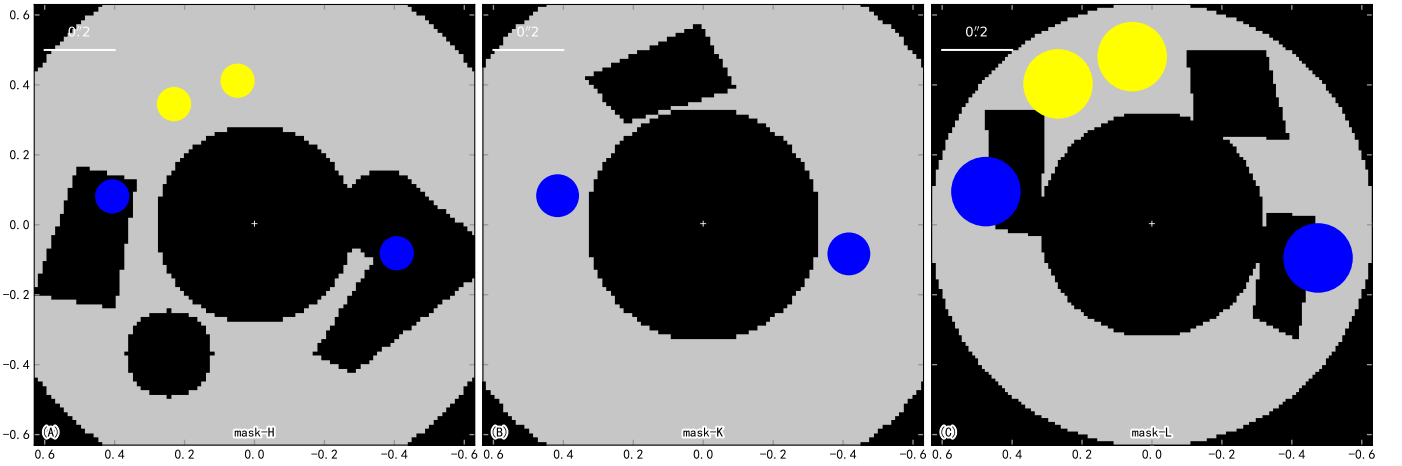


**Fig. A.1.** The masks used in forward modeling. The black region was masked excluded when calculating the likelihood function in Eq. (1). The blue circle masked the region where we calculated average disk surface brightness for disk in the major axis, and the yellow circle masked the region where we calculated average disk surface brightness for disk out of the major axis to avoid the affect of the shadow.

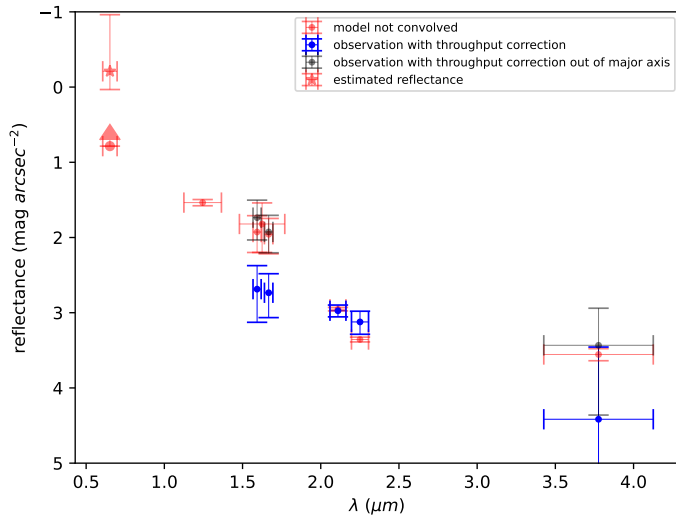


**Fig. A.2.** The reflectance of different bands and different methods of J1604. Notably, the black and blue points are overlapped with each other in the  $K1$  band. We presented the relative reflectance values expressed in units of  $\text{mag arcsec}^{-2}$ , where magnitude is calculated as  $-2.5 \log_{10} f_{\text{ref}}$  with  $f_{\text{ref}}$  representing reflectance ratio. Notably, we obtained the polarized disk intensity instead of the total intensity in the  $R$ -band, thus we provided a lower limitation for the reflectance in the  $R$ -band.

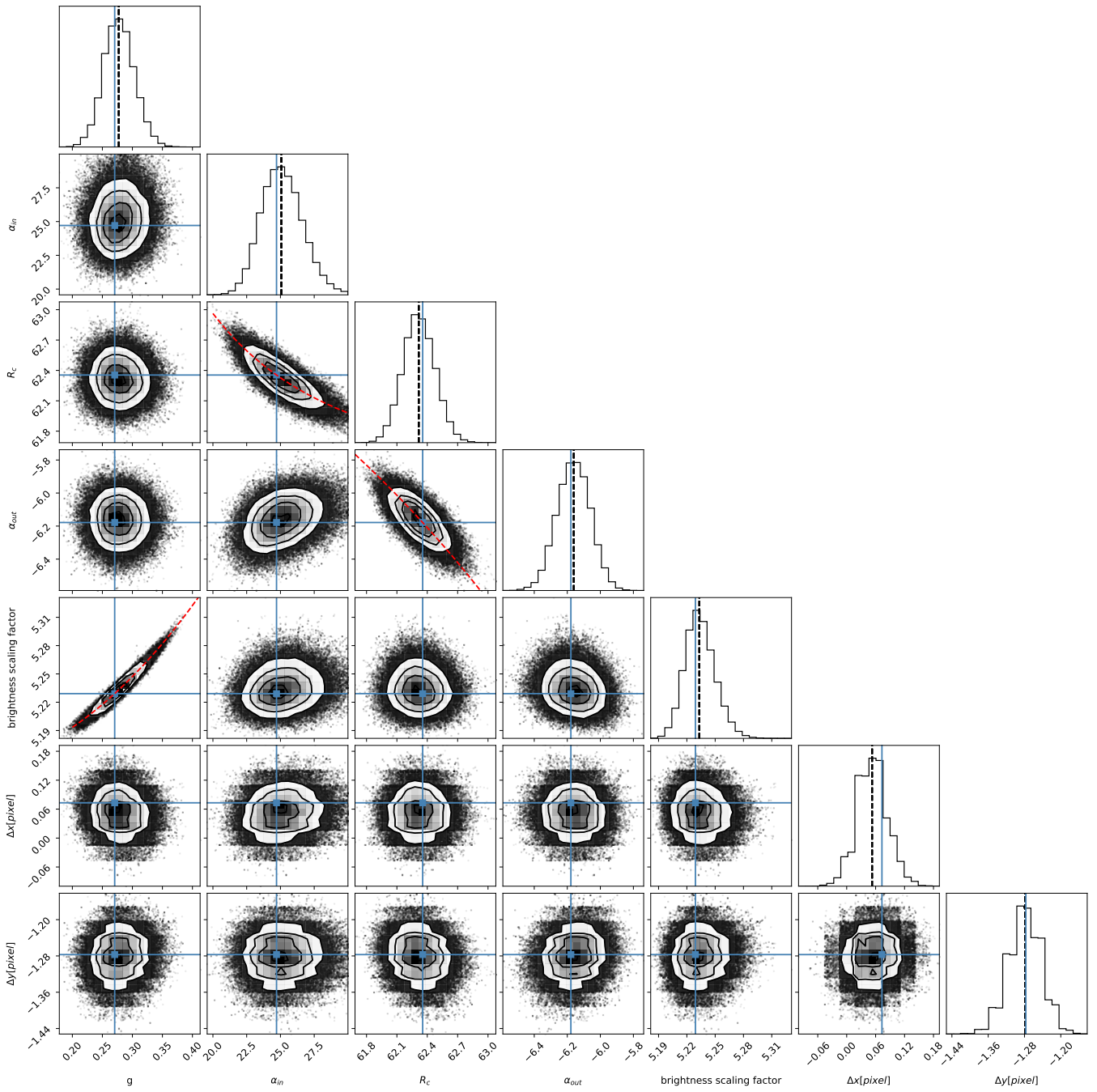


**Fig. A.3.** MCMC posteriors from forward modeling J1604 in  $H3$ -band.